Recovery of nonseparability in self-healing vector Bessel beams

Eileen Otte,[1] Isaac Nape,[2] Carmelo Rosales-Guzmán,[2,*] Adam Vallés,[2] Cornelia Denz,[1] and Andrew Forbes[2]
[1]*Institute of Applied Physics, University of Muenster, Corrensstr. 2/4, D-48149 Muenster, Germany*
[2]*School of Physics, University of the Witwatersrand, Private Bag 3, Wits 2050, South Africa*

(Received 21 May 2018; published 12 November 2018)

One of the most captivating properties of diffraction-free optical fields is their ability to reconstruct upon propagation in the presence of an obstacle, both classically and in the quantum regime. Here we demonstrate that the local entanglement, or nonseparability, between the spatial and polarization degrees of freedom also experience self-healing. We measured and quantified the degree of nonseparability between the two degrees of freedom when propagating behind various obstructions, which were generated digitally. Experimental results show that even though the degree of nonseparability reduces after the obstruction, it recovers to its maximum value within the classical self-healing distance. To confirm our findings, we performed a Clauser-Horne-Shimony-Holt Bell-like inequality measurement, proving the self-reconstruction of nonseparability. These results indicate that local entanglement between internal degrees of freedom of a photon, can be recovered by suitable choice of the enveloping wave function.

DOI: 10.1103/PhysRevA.98.053818

I. INTRODUCTION

Self-healing is one of the most fascinating properties of diffraction-free optical fields [1]. These fields have the ability to reconstruct if they are partially disturbed by an obstruction placed in their propagation path. Diffraction-free beams have found applications in fields such as imaging [2–4], optical trapping [5–8], laser material processing [9], among many others. Arguably, the most well-known propagation invariant (self-healing) fields are Bessel modes of light, first introduced in 1987 by Durin [1,10]. However, the self-healing property is not limited to so-called nondiffracting beams, but also appears in helico-conical [11], caustic, or self-similar fields, namely Airy [12], Pearcey [13], Laguerre-Gaussian [14,15], and even standard Gaussian beams [16]. Furthermore, within recent years, it has been shown that self-healing can also be observed at the quantum level, for example, McLaren *et al.* demonstrated experimentally the self-reconstruction of quantum entanglement [17]. Importantly, self-healing is not only an attribute of scalar fields but it can also apply to beams with spatially variant polarization [18–20].

Bessel beams also appear as complex vector light fields, where polarization and spatial shape can be coupled in a nonseparable way [21–23]. This property has fueled a wide variety of applications, from industrial processes, such as drilling or cutting [9,24,25], to optical trapping [26–31], high resolution microscopy [32], quantum and classical communication [33–35], among many others. Controversially, such nonseparable states of classical light are sometimes referred to as classically or nonquantum entangled [36]. This stems from the fact that the quintessential property of quantum entanglement is nonseparability, which is not limited to quantum systems. Indeed, the equivalence has been shown to be more than just a mathematical construct [34]. While such classical nonseparable fields do not exhibit nonlocality, they manifest all other properties of local entangled states.

Here, we demonstrate that the decay in such local entanglement after an obstruction can be counteracted if the carried field is Bessel. We create higher-order vector Bessel beams that are nonseparable in orbital angular momentum (the azimuthal component of the spatial mode) and polarization, and show that self-healing also comprises the nonseparability of the beams. This is at a first glance surprising since self-healing is traditionally attributed to the radial component of the spatial mode, which in our field is entirely separable. In order to demonstrate the far-reaching concept of self-healing, we unambiguously quantify the degree of nonseparability in different scenarios ranging from fully to partially reconstructed fields by performing a state tomography on the classical field [37,38]. We show both theoretically and experimentally that even though the nonseparability reduces after the obstruction, it recovers again upon propagation, proportionally to the level of self-reconstruction. Further, we confirm our findings by a Bell-like inequality measurement [39] in its most commonly used version for optics, namely, the Clauser-Horne-Shimony-Holt (CHSH) inequality [40], confirming that the nonseparability of vector Bessel beams also features self-healing properties. Although our tests are exerted on purely classical fields, the results are expected to be identical for the local entanglement of internal degrees of freedom of a single photon, and may be beneficial where such entanglement preservation is needed, e.g., transporting single photons through nanoapertures for plasmonic interactions.

II. VECTOR BESSEL MODES

A. Bessel-Gaussian beams

Over finite distances, a valid approximation of Bessel beams is given by the so-called Bessel-Gaussian (BG)

*carmelorosalesg@gmail.com

modes [41]. Besides other properties, these BG fields have the same ability of self-reconstruction in amplitude and phase [6,42]. In polar coordinates (r, φ, z), BG modes are defined as

$$E_\ell^{\mathrm{BG}}(r,\varphi,z) = \sqrt{\frac{2}{\pi}} J_\ell\left(\frac{z_R k_r r}{z_R - iz}\right) \exp\left(i\ell\varphi - ik_z z\right) \times \exp\left(\frac{ik_r^2 z w_0 - 2kr^2}{4(z_R - iz)}\right), \quad (1)$$

whereby ℓ represents the azimuthal index (topological charge), and k_r and k_z are the radial and longitudinal wave numbers, respectively. Further, $J_\ell(\cdot)$ defines the Bessel function, whereas the Gaussian information is encoded in the last factor with the initial beam waist w_0 of the Gaussian profile and the Rayleigh range $z_R = \pi w_0^2/\lambda$, λ being the wavelength. The finite propagation distance of BG modes ("nondiffracting length") is limited by $z_{\max}$. This distance describes the length of a rhombus-shaped region created by the superposition of plane waves with wave vectors lying on a cone described by the angle $\alpha = k_r/k$ (wave number $k = 2\pi/\lambda$) [41], as indicated in Fig. 1(a). The center of the rhombus-shaped region is positioned at z_0. For small α, i.e., $\sin\alpha \approx \alpha$, the nondiffracting distance is given by $z_{\max} = 2\pi w_0/\lambda k_r$ [5]. If an obstruction is included within the nondiffracting distance, a shadow region is formed of length $z_{\min} \approx R/\alpha \approx \frac{2\pi R}{k_r \lambda}$ [43] [Fig. 1(a)]. Here, R describes the radius of the obstruction. After this distance $z_{\min}$, the beam starts to recover due to the plane waves passing the obstruction [6,42]. A fully reconstructed BG beam will be observed at $2z_{\min}$, as visualized in Fig. 1(a).

B. Realization of obstructed BG modes

An established tool for the realization of complex beams are spatial light modulators (SLMs). These modulators allow for an on-demand dynamic modulation of structured beams by computer generated holograms [44]. For the formation of BG modes, we choose a binary Bessel function as phase-only hologram, defined by the transmission function,

$$T(r,\varphi) = \mathrm{sgn}\{J_\ell(k_r r)\}\exp(i\ell\varphi), \quad (2)$$

with the sign function $\mathrm{sgn}\{\cdot\}$ [45,46]. This approach has the advantage of generating a BG beam immediately after the SLM. An example of this function is shown in Fig. 1(b1). Note that for encoding this hologram we use a blazed grating [see Fig. 1(b2)], so that the desired beam is generated in the first diffraction order of the grating [47].

Here, we set $k_r = 18\,\mathrm{rad\,mm^{-1}}$ and $\ell = 0$ for the fundamental Bessel mode. Furthermore, we multiply the hologram by a Gaussian aperture function for the realization of a Gaussian envelope with $w_0 = 0.89\,\mathrm{mm}$ [see Eq. (1), Fig. 1(b2)]. These settings result in a BG beam with $z_{\max} = 49.16\,\mathrm{cm}$ for a wavelength of $\lambda = 633\,\mathrm{nm}$, whose intensity profile in the z_0 plane is depicted in Fig. 1(c).

Beyond the generation of BG modes, the SLM can also be used for the realization of obstructions within the z_0 plane [see Fig. 1(d1)]: Absorbing obstacles are created by including a circular central cut in the hologram, such that within this area no blazed grating is applied. This means the respective information of the BG mode is deleted in the first diffraction order. Furthermore, phase obstructions can be realized by adding the chosen phase object to the hologram. Hence, this artificial generation of obstructions facilitates the realization of any chosen kind of obstacle of defined radius R in the z_0 plane. Moreover, the relation $z_{\min} \approx \frac{2\pi R}{k_r \lambda}$ shows that a decrease in the radius R of the circular obstruction at z_0 results in a decrease in the length $z_{\min}$ of the shadow region, which is equivalent to moving the detection plane in the $\pm z$ direction [see Fig. 1(d2)], in order to analyze the evolution from a partially to a fully reconstructed beam.

C. Self-healing vector Bessel modes

In order to investigate the relation between the self-healing of propagation invariant beams and the nonseparability of light modes, we apply vector Bessel beams, or, more precisely, vector Bessel-Gaussian (vBG) modes. These modes are classically entangled in their spatial and polarization degrees of freedom (DoF) as explained in the next section. As illustrated in Fig. 1(d1), these beams are generated by a suitable combination of an SLM (SLM_1), half wave plates ($\frac{\lambda}{2}$) and a q-plate (q), a device capable of correlating the polarization and spatial DoFs [48]. First, we create the fundamental scalar BG mode (linearly polarized in the horizontal direction) by encoding the binary Bessel hologram [Fig. 1(b2)] on SLM_1. Within a $4f$ system we filter the first diffraction order with an aperture (A). If we now position, for example, a half wave plate, whose fast axis is oriented in a 45° ($\pi/4$) angle with respect to the incoming horizontal polarization, in combination with a q-plate ($q = 1/2$) in the beam path, an azimuthally polarized vBG mode is created in the image plane of SLM_1 [see Fig. 1(d1)]. The desired mode is generated from the q-plate by coupling the polarization DoF with the orbital angular momentum (OAM) via a geometric phase control, imprinting an OAM charge of $\pm 2q$ per circular polarization basis to the passing beam [48]. Note that wave and q-plate(s) do not need to be placed within the nondiffracting distance as we work in the paraxial regime ($\sin\alpha \approx \alpha$). The plates could even be located within the Fourier plane of SLM_1 [18]. Moreover, we are of course not limited to azimuthally polarized vBG modes. Depending on the chosen number and orientation of wave plates, different polarization structures are accessible [49] as depicted in Fig. 2. Here, we demonstrate the intensity distribution of different vBG beams in the z_0 plane analyzed by a polarizer (orientation indicated by white arrows).

In Fig. 1(e1) we present the experimentally measured propagation invariant properties of these modes by the example of the azimuthal vBG beam [cf. Fig. 2(a)]. The transverse intensity profile is shown for different positions $z \in [z_0, z_{\max}]$. Consider that the outer rings of the vBG mode disappear with increasing z due to the rhombus shape of the nondiffracting region.

As explained above, SLM_1 enables the inclusion of an obstruction within the holographically created scalar BG field. Following this, we are also able to apply the SLM for imparting an obstruction within the vBG mode: As SLM_1 is imaged by a $4f$ system to the z_0 plane of the vBG beam, an obstacle created by SLM_1 is also imaged to the z_0 plane of the formed vector mode [cf. Fig. 1(d1)]. As an example, we

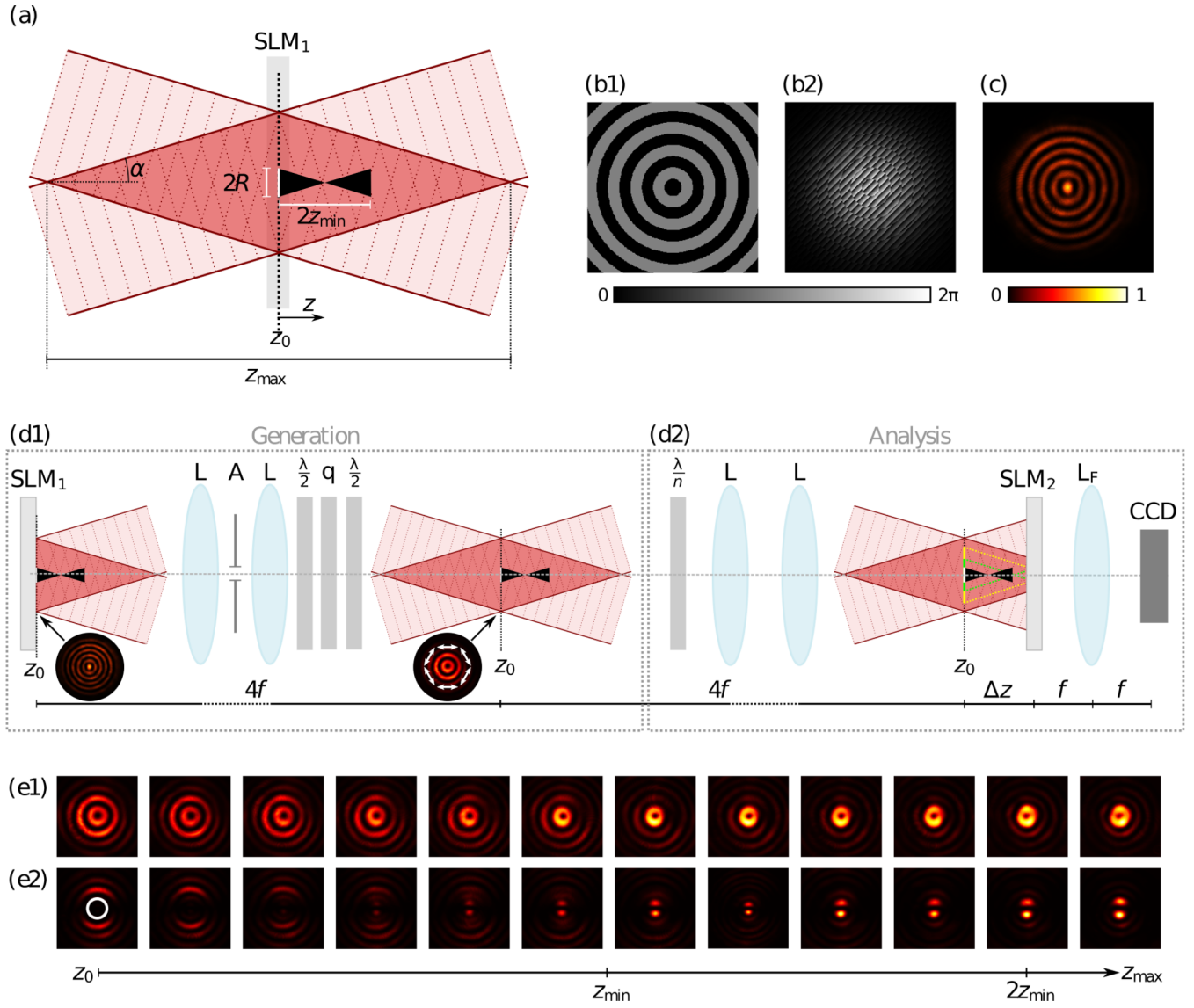

FIG. 1. (a) Formation of Bessel beams by off-axis interfering plane waves. If obstacles are included (radius R) a shadow region is formed. Scalar BG modes [intensity profile at z_0 in (c)] are realized by applying the binary Bessel function (b1) in combination with a blazed grating and Gaussian aperture (b2). (d) Concept of the realization and analysis of nonseparable vBG modes (SLM, spatial light modulator; $L_{(\mathcal{F})}$, (Fourier) lens with focal distance f; A, aperture; λ/n, $n = \{2, 4\}$, wave plates; q, q-plate; CCD, camera). (e) Propagation behavior of azimuthal vBG mode (e1) without obstruction and (e2) obstructed by on-axis absorbing object with $R = 200\,\mu$m, indicated by white circle.

investigated the propagation properties of the azimuthal vBG mode if obstructed by an absorbing object with $R = 200\,\mu$m created by SLM_1. Here, we included an additional horizontally oriented polarizer to analyze the polarization properties simultaneously. Results are shown in Fig. 1(e2). For the programmed obstacle we calculate a self-healing distance of $z_{\min} = 11.02\,$cm. The shown intensity distributions reveal a self-reconstruction of the beam including its polarization properties after approximately $2z_{\min}$, as expected.

III. LOCAL ENTANGLEMENT IN SELF-HEALING OPTICAL BEAMS

A. Local entanglement in classical optics

For the benefit of the reader, in this section we briefly introduce the notion of local entanglement in classical optics and its relevance to this study. Entanglement is commonly regarded as a property of quantum systems. However, in recent time several works have demonstrated that entanglement is of a more general nature that also includes classical systems[50–55]. Entanglement can happen in two different ways: between systems that are spatially separated from each other or between the internal DoF of a system, denoted as nonlocal or local, respectively. While the first one can only be used in a quantum context, the second, local entanglement, applies as well to classical systems, for example, to the nonseparability between polarization and spatial DoF in vector beams, an example of a bipartite system [56–61]. In this context, two systems A and B are nonseparable or classically entangled if they cannot be represented as a factorizable product of the two subsystems, i.e., $|\Psi_{AB}\rangle \neq |A\rangle \otimes |B\rangle$. Here, the symbol $\otimes$ denotes the tensor product of the two DoF.

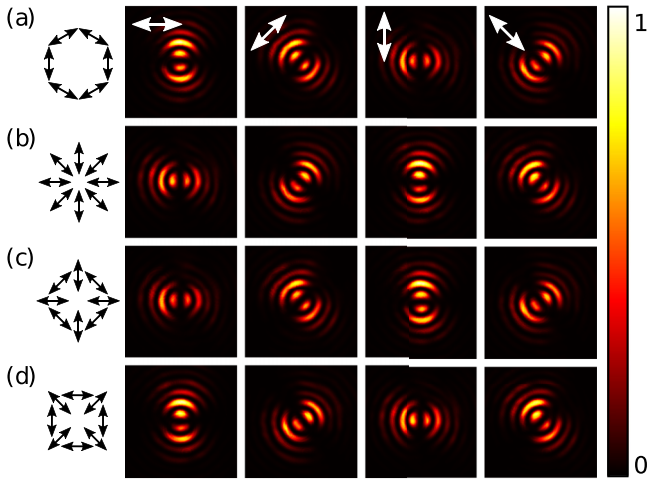

FIG. 2. Examples of nonseparable vBG modes with respective polarization analysis. The normalized intensity distribution in the z_0 plane for different orientations of a polarizer are shown. The respective orientation is indicated by white arrows in (a). The according polarization distribution is highlighted by black arrows.

In a similar way to quantum systems, local classical entanglement or nonseparability can be quantified by the level of crosstalk when decomposed into a basis of observables with maximal nonseparability [37,62]. To show this, let us take the example of a vector beam, expressed using Dirac's notation [23,37,63],

$$|\psi\rangle = \sqrt{a}|u_R\rangle \otimes |R\rangle + \sqrt{(1-a)}|u_L\rangle \otimes |L\rangle, \qquad (3)$$

where the ket $|u_R\rangle$ and $|u_L\rangle$ represents the spatial DoF, the kets $|R\rangle$ and $|L\rangle$ represent the polarization DoF in the right-left circular basis. The weighting factors $\sqrt{a}$ and $\sqrt{1-a}$, with $a \in [0, 1]$, determine the degree of local entanglement, ranging from 0 for separable (nonentangled) to 1 for nonseparable (entangled) states.

According to quantum mechanics, the degree of entanglement of a pure state of bipartite systems can be quantified through the entanglement entropy [64]. More explicitly, this is given by the von Neumann entropy of the reduced density matrix of the polarization DoF, obtained by tracing over the spatial DoF, as [37,65]

$$E(|\psi\rangle) = -\mathrm{Tr}[\rho_p \log(\rho_p)], \qquad \rho_p = \mathrm{Tr}_s[|\psi\rangle\langle\psi|]. \qquad (4)$$

This expression provides us with a means to measure entanglement with respect to the degree of mixedness of the polarization DoF. Physically, the reduced density matrix,

$$\rho_p = \begin{pmatrix} a & \sqrt{a(1-a)}|u_L\rangle\langle u_R| \\ \sqrt{a(1-a)}|u_R\rangle\langle u_L| & (1-a) \end{pmatrix}, \qquad (5)$$

determines the average polarization of the classically entangled state and can be determined by measuring the components $s_i = \mathrm{Tr}[\sigma_i \rho_p]$, $i = \{1, 2, 3\}$, of the Bloch vector $\mathbf{s}$. The terms $\rho_p = (\mathbb{1} + \sum_i s_i \sigma_i)/2$ correspond to the Stokes parameters, and σ_i are the traceless Pauli operators spanning the so-called higher-order Poincaré sphere (HOPS; see Fig. 3) [66].

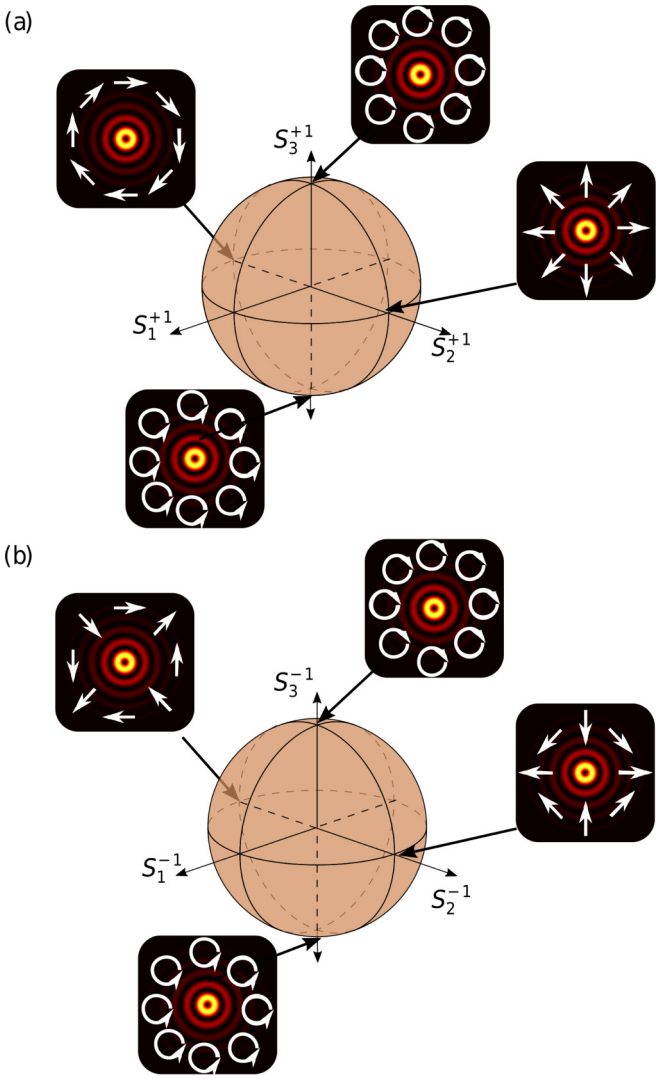

FIG. 3. Higher-order Poincaré spheres of self-healing BG beams spanned by the Stokes parameters (a) $S_{1,2,3}^{+1}$ for $\mathcal{H}_{2,\sigma,\ell=1}$ and (b) $S_{1,2,3}^{-1}$ for $\mathcal{H}_{2,\sigma,\ell=-1}$. The poles represent separable BG states with circular polarization and $\ell = \pm 1$, while nonseparable vBG states are found on the equator (i.e., the plane intersecting the $S_{1,2}^{\pm 1}$ plane).

These operators are given by

$$\begin{aligned} \sigma_1 &= |H\rangle\langle H| - |V\rangle\langle V|, \\ \sigma_2 &= \frac{1}{2}(|H+V\rangle\langle H+V| - |H-V\rangle\langle H-V|), \\ \sigma_3 &= |R\rangle\langle R| - |L\rangle\langle L|. \end{aligned} \qquad (6)$$

The classical entanglement is thus calculated as

$$E = -\left(\frac{1+s}{2}\right)\log\left(\frac{1+s}{2}\right) - \left(\frac{1-s}{2}\right)\log\left(\frac{1-s}{2}\right), \qquad (7)$$

where s is the length of the Bloch vector and is given by

$$s(\rho_P) = \left(\mathrm{Tr}\left[\rho_P^2\right]\right)^{1/2} = \left(\sum_{i=1}^{3}\langle\sigma_i\rangle\right)^{1/2}. \qquad (8)$$

To quantify the degree of classical entanglement or nonseparability, we can rely on the closely related concurrence C and define its real part as the vector quality factor (VQF) or vectornes [62], namely

$$\mathrm{VQF} = \mathrm{Re}(C) = \mathrm{Re}(\sqrt{1-s^2}). \tag{9}$$

In the following, we employ the VQF measure as a figure of merit for determining the nonseparability of partially obstructed and consequently self-healing vBG modes.

B. Vector quality factor of obstructed beams

Following the description in Eq. (3), we consider an arbitrary self-healing vBG field with each photon described by the following state:

$$|\Psi\rangle_{k_r,\ell} = \cos(\theta)|u_{k_r,\ell}\rangle|R\rangle + \sin(\theta)|u_{k_r,-\ell}\rangle|L\rangle, \tag{10}$$

where polarizations $|R\rangle$ and $|L\rangle$ span the qubit Hilbert space $\mathcal{H}_2$. The infinite dimensional state vectors $|u_{k_r,\pm\ell}\rangle \in \mathcal{H}_\infty$ represent the self-healing transverse eigenstates, namely scalar Bessel or BG modes of light [cf. Eq. (1)], characterized by the continuous radial wave number k_r and the topological charge ℓ. Equivalently to a in Eq. (3), the parameter θ determines whether $|\Psi\rangle_{k_r\ell}$ is purely vector (nonseparable; $\theta = (2n+1)\pi/4,\ n \in \mathbf{Z}$), scalar (separable; $\theta = n\pi/2,\ n \in \mathbf{Z}$), or some intermediate state. Accordingly, the respective VQF is given by

$$\mathrm{VQF} = |\sin(2\theta)|. \tag{11}$$

From wave optics, it is well known that an obstructed beam can be modified in both phase and amplitude due to the interaction between the beam and the outer edges of an obstruction, resulting in diffraction. At the single photon level, this can be understood as modal coupling [67]. That is, if some field with a transverse profile given by $|u_{k_{r_1},\ell_1}\rangle$ interacts with an obstruction, the state evolves following the mapping,

$$\left|u_{k_{r_1},\ell_1}\right\rangle \rightarrow \int \sum_\ell \alpha_\ell(k_r)\left|u_{k_r,\ell}\right\rangle dk_r, \tag{12}$$

where the input mode spreads over all eigenmodes $|u_{k_r,\ell}\rangle$. The coefficients $|\alpha_\ell(k_r)|^2$ represent the probability of the state $|u_{k_{r_1},\ell_1}\rangle$ scattering into the eigenstates $|u_{k_r,\ell}\rangle$ with the property that $\int \sum_\ell |\alpha_\ell(k_r)|^2 dk_r = 1$. Applying the mapping of Eq. (12) to the scattering of the self-healing vBG mode presented in Eq. (10) and post-selecting particular k_r and ℓ values yields the state,

$$\begin{aligned}|\Phi_{k_r,\ell}\rangle = {} & a|u_{k_r,\ell}\rangle|R\rangle + b|u_{k_r,-\ell}\rangle|R\rangle \\ & + c|u_{k_r,}\rangle|L\rangle + d|u_{k_r,\ell}\rangle|L\rangle,\end{aligned} \tag{13}$$

where $|a|^2 + |b|^2 + |c|^2 + |d|^2 = 1$. Consequently, $|\Phi_{k_r,\ell}\rangle$ restricts the measurement of the photons to the four-dimensional Hilbert space $\mathcal{H}_4 = \mathrm{span}(\{|R\rangle, |L\rangle\} \otimes \{|u_{k_r,\ell}\rangle, |u_{k_r,-\ell}\rangle\})$ which can be written as the direct sum,

$$\mathcal{H}_4 = \mathcal{H}_{2,\sigma,\ell} \oplus \mathcal{H}_{2,\sigma,-\ell}. \tag{14}$$

The subspaces $\mathcal{H}_{2,\sigma,\pm\ell} = \mathrm{span}(|u_{k_r,\pm\ell}\rangle|R\rangle, |u_{k_r,\mp\ell}\rangle|L\rangle)$ are topological unit spheres for spin-orbit coupled beams belonging to the family of HOPS [66].

Invoking the equivalence between VQF and concurrence enables us to exploit the definition of concurrence with $C = \sqrt{(1 - \mathrm{Tr}(\sqrt{\rho_p}))}$ for a given density matrix ρ_ψ where ρ_p is the reduced density matrix. In quantum mechanics, if the state of a two-qubit system written in the logical computation basis is given by the pure state,

$$|\Psi\rangle = c_1|0\rangle|0\rangle + c_2|0\rangle|1\rangle + c_3|1\rangle|0\rangle + c_4|1\rangle|1\rangle, \tag{15}$$

satisfying the normalization condition $\sum_{j=1}^4 |c_j|^2 = 1$, the concurrence is $C = 2|c_1c_4 - c_3c_2|$. By replacing the two-qubit logical basis with the $\mathcal{H}_4$ basis from the two HOPSs, we can equivalently write the VQF as

$$\mathrm{VQF} = 2|ad - cb|, \tag{16}$$

following Eq. (13).

As an illustrative example, consider the azimuthally polarized vBG mode given by

$$|\psi\rangle_{k_r,1} = \frac{1}{\sqrt{2}}(|u_{k_r,1}\rangle|R\rangle - |u_{k_r,-1}\rangle|L\rangle). \tag{17}$$

Upon diffracting off the edges of an obstruction, one expects the mode coupling profiled in Eq. (13) to occur (by restricting $|\ell| = 1$). However, since the radial profile of BG modes enables the transverse structure to self-heal, $cb \rightarrow 0$ and $ad \rightarrow -\frac{1}{2}$, and therefore VQF $\rightarrow 1$ giving rise to the self-healing of the nonseparability. This behavior is predicated to occur best after twice of the minimum self-healing distance $z_{\min}$.

To experimentally quantify the characteristics of vectorness, i.e., classical entanglement, in relation to the self-healing properties of vGB modes, we apply a configuration as indicated in Fig. 1(d2). By this configuration, consisting of a quarter wave plate ($\frac{\lambda}{n}$, $n = 4$), a polarization sensitive SLM (SLM$_2$), a Fourier lens ($\mathrm{L}_\mathcal{F}$), and a CCD camera, we determine the expectation values of the Pauli operators $\langle\sigma_i\rangle$, $i = \{1, 2, 3\}$ by 12 on-axis intensity measurements or six identical measurements for two different basis states [37,38]. These values are used to determine the VQF according to Eq. (9).

If circular polarization is chosen as basis $|R\rangle$, $|L\rangle$, the projection measurements represent two OAM modes of topological charge ℓ and $-\ell$, namely $|u_{k_r,\pm\ell}\rangle = E^{\mathrm{BG}}_{\pm\ell}$, as well as four superposition states $|u_{k_r,\ell}\rangle + \exp(i\gamma)|u_{k_r,-\ell}\rangle$ with $\gamma = \{0, \pi\ell/2, \pi\ell, 3\pi\ell/2\}$. As we use a q-plate with $q = 1/2$, our measurements are performed for $\ell = 1$. Following Table I, we calculate expectation values $\langle\sigma_i\rangle$ from

$$\begin{aligned}\langle\sigma_1\rangle &= I_{13} + I_{23} - (I_{15} + I_{25}),\\ \langle\sigma_2\rangle &= I_{14} + I_{24} - (I_{16} + I_{26}),\\ \langle\sigma_3\rangle &= I_{11} + I_{21} - (I_{12} + I_{22}).\end{aligned}$$

TABLE I. Normalized intensity measurements I_{uv} for the determination of expectation values $\langle\sigma_i\rangle$.

Basis states	$\ell = 1$	-1	$\gamma = 0$	$\pi/2$	π	$3\pi/2$
Left circular $\|L\rangle$	I_{11}	I_{12}	I_{13}	I_{14}	I_{15}	I_{16}
Right circular $\|R\rangle$	I_{21}	I_{22}	I_{23}	I_{24}	I_{25}	I_{26}

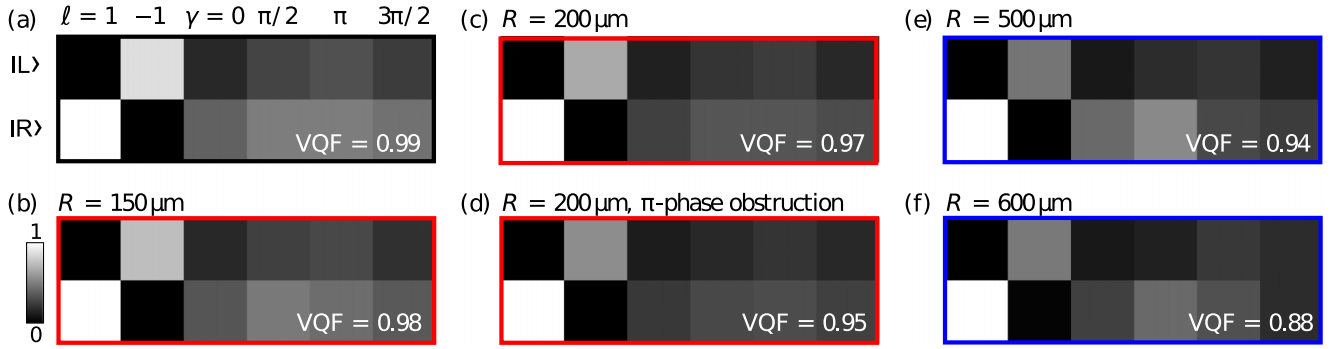

FIG. 4. Vector quality analysis of self-healing vBG mode (azimuthally polarized) without obstacle (a), with absorbing obstacles of radius (b) $R = 150\,\mu$m, (c) $R = 200\,\mu$m, (e) $R = 500\,\mu$m, and (f) $R = 600\,\mu$m, as well as (d) phase obstacle (homogeneous phase shift of π) of radius $R = 200\,\mu$m. Results for beams which (do not) fully self-heal before the analysis are marked (blue) red with respective VQF within the measured normalized matrices of on-axis intensity values arranged according to Table I.

On-axis intensity values I_{uv}, $u = \{1, 2\}$, $v = \{1, 2, ..., 6\}$, are normalized by $I_{11} + I_{12} + I_{21} + I_{22}$. The respective polarization projections are performed by inserting a quarter wave plate, set to $\pm 45^\circ$, in combination with the polarization selective SLM_2. Further, SLM_2 is responsible for the OAM projections. For this purpose, we encode the OAM as well as superposition states as phase-only holograms according to the binary Bessel function in Eq. (2). Finally, the on-axis intensity is measured in the focal plane of a Fourier lens by means of a CCD camera.

Crucially, the decoding SLM_2 is placed at an adequately chosen distance $\Delta z = 23\,$cm from the z_0 plane so that we are able to access different levels of self-healing without the need to move the detection system. That is, by changing the radius R of the digitally created obstruction, the vBG mode can fully self-heal in front of ($2z_{\min} < \Delta z$) or behind ($2z_{\min} > \Delta z$) this SLM_2, as indicated in Fig. 1(d2) by the black shadow region or the green and yellow dashed lines, respectively.

C. Experimental quantification of vectorness

First, we prove that pure undisturbed vBG modes show the maximum degree of nonseparability. This is exemplified by the analysis of an azimuthally polarized vBG beam. The experimentally measured on-axis intensity values are visualized in Fig. 4(a), arranged according to Table I. The measurements result in a VQF of 0.99, verifying our expectation. In a next step, we digitally impart different obstacles and determine the respective VQF. On the one hand, we chose obstacles allowing the beam to self-reconstruct within $\Delta z = 23\,$cm, namely absorbing obstructions with $R = 150\,\mu$m ($2z_{\min} = 2 \times 8.27\,\text{cm} = 16.54\,\text{cm}$) or $R = 200\,\mu$m ($2z_{\min} = 2 \times 11.03\,\text{cm} = 22.06\,\text{cm}$) and a phase obstacle with $R = 200\,\mu$m creating a homogeneous phase shift of π [Figs. 4(b)–4(d)]. On the other hand, we program absorbing obstructions with $R = 500\,\mu$m ($2z_{\min} = 2 \times 27.57\,\text{cm} = 55.14\,\text{cm}$) and $R = 600\,\mu$m ($2z_{\min} = 2 \times 33.03\,\text{cm} = 66.06\,\text{cm}$), for which $2z_{\min} > \Delta z$ and even $z_{\min} > \Delta z$ [Figs. 4(e) and 4(f)]. The respective measured VQFs are shown within each subfigure.

Obviously, the degree of nonseparability, i.e., the VQF, decreases with increasing absorbing obstacle size R (Fig. 4). For self-healed beams with absorbing obstacles [Figs. 4(b) and 4(c)], the VQF differs only minimally from the nonobstructed case (a). Note that a phase obstruction of the same radius (d) results in a slightly larger deviation. In contrast to absorbing obstacles, causing a loss of information, phase obstructions do not cut but vary information. Since in the case of absorbing obstacles the cut information is also included within the passing plane waves, the loss can be compensated within $2z_{\min}$. In the phase obstruction case, the varied information represents additional information, i.e., noise, within the nondiffracting beam, which is not eliminated when being decoded by the SLM. Hence, the beam stays disturbed and, as a consequence, the VQF decreases.

Further, if the beam cannot fully reconstruct before being decoded by SLM_2, thus, if we analyze the degree of entanglement within the self-healing distance [Figs. 4(e) and 4(f)], the decrease in VQF is relatively large in comparison to the self-healed versions in Figs. 4(b) and 4(c). However, note that in both cases, the self-reconstructed and nonreconstructed beams, the VQF is $\geqslant 0.88$. Consequently, the beams are closer to being vector or nonseparable (VQF = 1) than scalar or separable (VQF = 0). This is due to the fact that there is always undisturbed information reaching the SLM_2, and only little scattering into other modes, i.e., little modal coupling. We thus may conclude that the beam is always nonseparable, but due to noise caused by the obstacle the measurement shows deviations from pure nonseparability. As the noise is annihilated with propagation distance (for absorbing obstacles), the quantitative value for nonseparability, namely VQF, recovers. This effect is similar to what we call "self-healing" in the case of amplitude, phase, and polarization of vBG modes: Obstacles add noise to the information on these degrees of freedom. Upon propagation, these perturbations vanish and the pure vBG mode information is left so that the beam and its properties seem to self-reconstruct.

Consequently, we conclude that the lower the level of self-healing, i.e., the larger the obstacle, the smaller the VQF. This means, not only amplitude, phase, and polarization properties of the vBG mode reconstruct with distance behind an obstruction, but also the degree of nonseparability.

D. CHSH Bell-like inequality violation

To confirm our results with respect to the VQF, we performed an additional investigation of the degree of entan-

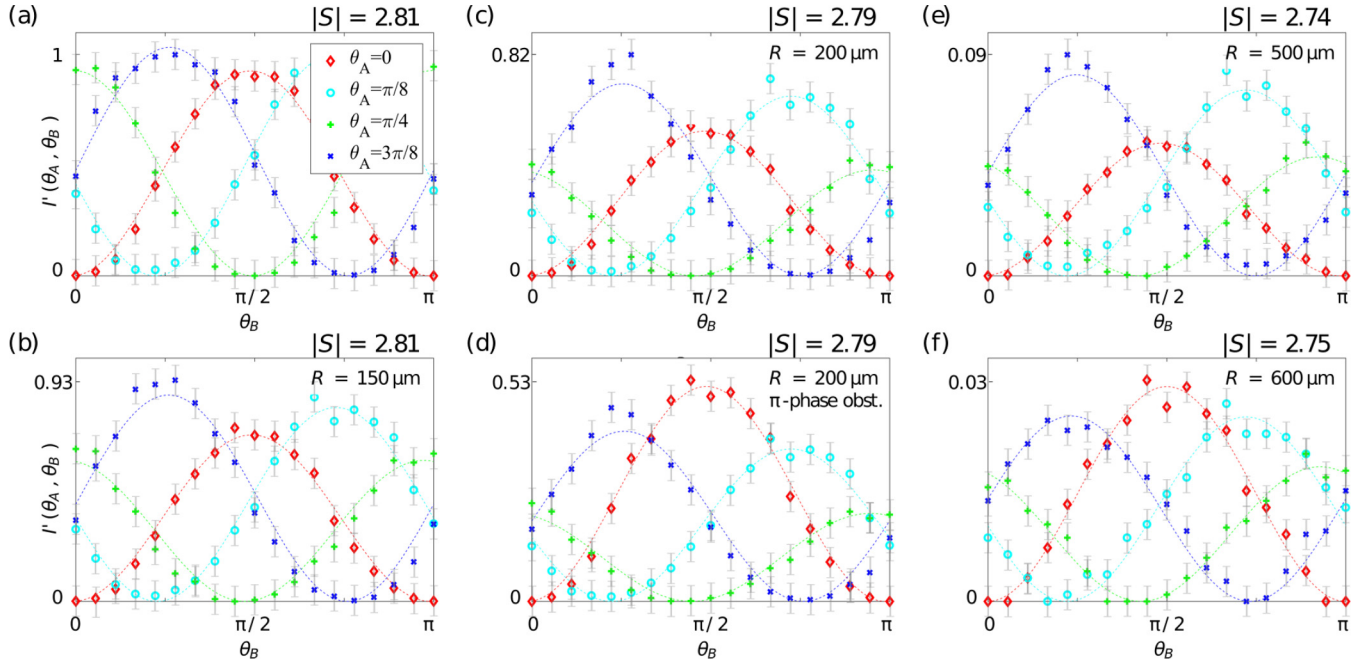

FIG. 5. Bell-type curves for azimuthal vBG mode with four different orientations $2\theta_A$ of the half wave plate to determine the Bell parameter $|S|$. The investigations were performed undisturbed (a) as well as for differently sized obstacles (radii $R = \{150,\ 200,\ 500,\ 600\}$ µm in (b)–(f)) and a π-phase obstacle ($R = 200$ µm) (d). Shown on-axis intensity measurements $I'(\theta_A, \theta_B)$ for (a)–(f) are normalized according to the maximum intensity measured without obstacle (a). Dashed curves represent $\cos^2$ fits used to determine S.

glement or nonseparability using the Bell parameter [37,61]. More specifically, we perform a Clauser-Horne-Shimony-Holt (CHSH) inequality measurement [40], the most commonly used Bell-like inequality for optical systems, to demonstrate the degree of entanglement between polarization and spatial DoFs. Instead of measuring a single DoF, e.g., polarization or OAM, nonlocally, we analyze two DoF locally on the same classical light field [37]. The veracity of this procedure for the study at hand is based on the analogy of local entanglement between classical and quantum systems [37,53,55,59,61,68], as outlined in Sec. III A. Importantly, classical and local nonseparability (entanglement) by definition cannot be nonlocal, so this aspect cannot be tested, but nor do we need to as all our measurements are local. For the respective measurement, we placed a half wave plate ($\frac{\lambda}{n}$, $n = 2$) in front of SLM_2 [see Fig. 1(d2)] and measured the on-axis intensity $I(\theta_A, \theta_B)$ for different angles $2\theta_A = \{0,\ \pi/8,\ \pi/4,\ 3\pi/4\}$ of the half wave plate. Here, $\theta_B \in [0,\ \pi]$ represents the rotation angle of the hologram encoded on SLM_2 by $|u_{k_r,\ell}\rangle + \exp(\mathrm{i}2\theta_B)|u_{k_r,-\ell}\rangle$ ($\ell = 1$, $k_r = 18\,\mathrm{rad\,mm^{-1}}$).

We define the CHSH-Bell parameter S as

$$S = E(\theta_A, \theta_B) - E(\theta_A, \theta'_B) + E(\theta'_A, \theta_B) + E(\theta'_A, \theta'_B), \tag{18}$$

with $E(\theta_A, \theta_B)$ being calculated from measured on-axis intensity according to [37]

$$\begin{aligned} E(\theta_A, \theta_B) &= \frac{A(\theta_A, \theta_B) - B(\theta_A, \theta_B)}{A(\theta_A, \theta_B) + B(\theta_A, \theta_B)}. \\ A(\theta_A, \theta_B) &= I(\theta_A, \theta_B) + I\left(\theta_A + \frac{\pi}{2}, \theta_B + \frac{\pi}{2}\right), \\ B(\theta_A, \theta_B) &= I\left(\theta_A + \frac{\pi}{2}, \theta_B\right) + I\left(\theta_A, \theta_B + \frac{\pi}{2}\right). \end{aligned} \tag{19}$$

The values of S ranges from $|S| \leqslant 2$ for separable states, up to $|S| = 2\sqrt{2}$ for entangled or nonseparable states, which is known as Tsirelson's bound [69]. Our experimental results with according Bell parameters $|S|$ are presented in Fig. 5. As before, we performed our investigation without obstacle [Fig. 5(a)] as well as with different absorbing obstacles of radii $R = \{150,\ 200,\ 500,\ 600\}$ µm [Figs. 5(b)–5(f)], or Fig. 5(d) phase obstructing. Note that the intensity values (mean of seven neighboring CCD pixel values) are normalized with respect to the maximum value measured in the unobstructed case ($I'(\theta_A, \theta_B)$). Considering the standard deviation as well as systematic and technical errors within the experiment, an error of ±7% of the maximum intensity in each graph Figs. 5(a)–5(f) ($I'_{\max}(R)$) is assumed. Obviously, the ratio of measurable maximum intensity $I'_{\max}(R)$ decreases dramatically depending on the size of the obstruction, as it can be seen on the $I'(\theta_A, \theta_B)$ axis (vertical) of Fig. 5. However, the Bell parameter does not change significantly if we measure in the fully reconstructed regime [$2z_{\min} < \Delta z$ for Figs. 5(b)–5(d)] compared to the undisturbed vBG mode (a). In accordance with our VQF analysis, $|S|$ reveals bigger changes if the beam is not fully self-healed when it is analyzed in Figs. 5(e) and 5(f). In total, even if the intensity lowers to some percentage [Fig. 5(f)] of the original maximum value [Fig. 5(a)], all measurements validate a violation of the Bell inequality, matching our nonseparability analysis results based on vectorness.

E. The relation of self-healing and nonseparability

In Table II we summarize our results emphasizing the dependence of the VQF, the maximum intensity $I'_{\max}$ as well as Bell parameter $|S|$ on the size R of included obstructions, i.e., on the self-healing level. The maximum intensity $I'_{\max}(R)$

TABLE II. Quantification of nonseparability properties of self-reconstructing vBG modes as a function of the self-healing level, given by the obstacle radius R.

R in μm	0	150	200	200, π obst.	500	600
VQF	0.99	0.98	0.97	0.95	0.94	0.88
$\|S\|$	2.81	2.81	2.79	2.79	2.74	2.75
$I'_{\max}$	1	0.93	0.82	0.53	0.09	0.03

reveals an approximately Gaussian decrease with increasing obstacle size which reflects the Gaussian envelope of investigated vBG mode. Simultaneously to the intensity, the VQF as well as $|S|$ decrease as demonstrated in previous sections. However, only small changes are observed as only minor noise is disturbing vBG modes if obstructions are included. In short, both vector quality as well as Bell analysis reveal a similar behavior of nonseparability with respect to changes in the obstruction size, demonstrating the self-healing of the degree of entanglement within obstructed vBG beams.

IV. CONCLUSION AND DISCUSSION

It is well known that the phase and amplitude of vector Bessel beams self-heal in the presence of an obstacle that partially blocks its path. However, there are no reports about the effect of this on the coupling between phase and polarization, known as classical entanglement. In this work, we presented for the first time to our knowledge experimental evidence that even though the coupling between these two degrees of freedom decreases after passing an obstruction, it eventually restores itself to its maximum value. For this purpose, we dynamically realized vector Bessel Gaussian (vBG) modes with digital obstructions by combining holography-based generation of structured light with a q-plate. We quantified the degree of nonseparability between the spatial shape and polarization using two different means: the vector quality factor (VQF) and a classical version of the CHSH Bell-like inequality. By a specific design of our detection system combined with digital variation of the obstruction size, different levels of self-healing were accessible, which enabled the relation between degree of nonseparability and self-healing level to be analyzed. The measured VQF values showed that the degree of classical entanglement increases as a function of decreasing object size. Analogously, the measured CHSH S parameter values show a similar dependence on the object size or self-healing level of the vBG beam, showing in all cases a clear violation of the CHSH inequality. This behavior can be interpreted as self-healing in the degree of nonseparability as a function of the distance from an obstacle since a decrease in obstacle size is comparable to placing the detector farther from the object. Physically, our findings can be described by the annihilation of perturbation with propagation distance within a nonseparable beam: Even though an obstacle cuts or adds noise to the light field, there is always undisturbed information kept in passing plane waves. Upon propagation, the loss of information is compensated or the noise is canceled by these waves so that quantitative values for nonseparability recover.

The complex fields used in this study were separable in radial profile, defined by the k_r vector of the conical waves, but nonseparable in the azimuthal profile and polarization, the latter being defined by the OAM of each polarization component. Intriguingly, it is the radial profile that leads to the self-healing of the nonseparability, despite itself being separable. Thus the local entanglement in angular momentum (spin and OAM) can be made more resilient to decay from obstructions by engineering the unused degree of freedom in a judicious manner.

ACKNOWLEDGMENTS

E.O. acknowledges financial support from the German Research Foundation DFG (EXC 1003 - CiM, TRR61), I.N. from the Department of Science and Technology (South Africa), and A.V. from the Claude Leon Foundation.

[1] J. Durnin, J. J. Miceli, and J. H. Eberly, Phys. Rev. Lett. **58**, 1499 (1987).
[2] F. O. Fahrbach, P. Simon, and A. Rohrbach, Nat. Photonics **4**, 780 (2010).
[3] T. A. Planchon, L. Gao, D. E. Milkie, M. W. Davidson, J. A. Galbraith, C. G. Galbraith, and E. Betzig, Nature Methods **8**, 417 (2011).
[4] F. O. Fahrbach and A. Rohrbach, Nat. Commun. **3**, 632 (2012).
[5] D. McGloin and K. Dholakia, Contemp. Phys. **46**, 15 (2005).
[6] D. McGloin, V. Garcés-Chávez, and K. Dholakia, Opt. Lett. **28**, 657 (2003).
[7] J. Arlt, V. Garces-Chavez, W. Sibbett, and K. Dholakia, Opt. Commun. **197**, 239 (2001).
[8] K. Volke-Sepulveda, V. Garcés-Chávez, S. Chávez-Cerda, J. Arlt, and K. Dholakia, J. Opt. B: Quantum Semiclassical Opt. **4**, S82 (2002).
[9] A. K. Dubey and V. Yadava, International Journal of Machine Tools and Manufacture **48**, 609 (2008).
[10] J. Durnin, J. Opt. Soc. Am. A **4**, 651 (1987).
[11] N. Hermosa, C. Rosales-Guzmán, and J. P. Torres, Opt. Lett. **38**, 383 (2013).
[12] J. Broky, G. A. Siviloglou, A. Dogariu, and D. N. Christodoulides, Opt. Express **16**, 12880 (2008).
[13] J. D. Ring, J. Lindberg, A. Mourka, M. Mazilu, K. Dholakia, and M. R. Dennis, Opt. Express **20**, 18955 (2012).
[14] Z. Bouchal, Opt. Commun. **210**, 155 (2002).
[15] J. Mendoza-Hernández, M. L. Arroyo-Carrasco, M. D. Iturbe-Castillo, and S. Chávez-Cerda, Opt. Lett. **40**, 3739 (2015).
[16] A. Aiello, G. S. Agarwal, M. Paúr, B. Stoklasa, Z. Hradil, J. Řeháček, P. de la Hoz, G. Leuchs, and L. L. Sánchez-Soto, Opt. Express **25**, 19147 (2017).
[17] M. McLaren, T. Mhlanga, M. J. Padgett, F. S. Roux, and A. Forbes, Nat. Commun. **5**, 3248 EP (2014).

[18] G. Milione, A. Dudley, T. A. Nguyen, O. Chakraborty, E. Karimi, A. Forbes, and R. R. Alfano, J. Opt. **17**, 035617 (2015).
[19] G. Wu, F. Wang, and Y. Cai, Phys. Rev. A **89**, 043807 (2014).
[20] P. Li, Y. Zhang, S. Liu, H. Cheng, L. Han, D. Wu, and J. Zhao, Opt. Express **25**, 5821 (2017).
[21] Q. Zhan, Adv. Opt. Photonics **1**, 1 (2009).
[22] C. Rosales-Guzmán, N. Bhebhe, and A. Forbes, Opt. Express **25**, 25697 (2017).
[23] E. Otte, C. Rosales-Guzmán, B. Ndagano, C. Denz, and A. Forbes, Light: Sci. Appl. **7**, 18009 (2018).
[24] M. Meier, V. Romano, and T. Feurer, Appl. Phys. A **86**, 329 (2007).
[25] V. G. Niziev and A. V. Nesterov, J. Phys. D **32**, 1455 (1999).
[26] M. G. Donato, S. Vasi, R. Sayed, P. H. Jones, F. Bonaccorso, A. C. Ferrari, P. G. Gucciardi, and O. M. Maragó, Opt. Lett. **37**, 3381 (2012).
[27] Y. Zhao, Q. Zhan, Y. Zhang, and Y.-P. Li, Opt. Lett. **30**, 848 (2005).
[28] Q. Zhan, Opt. Express **12**, 3377 (2004).
[29] B. Roxworthy and K. Toussaint, New J. Phys. **12**, 073012 (2010).
[30] Y. Kozawa and S. Sato, Opt. Express **18**, 10828 (2010).
[31] L. Huang, H. Guo, J. Li, L. Ling, B. Feng, and Z.-y. Li, Optics letters **37**, 1694 (2012).
[32] P. Török and P. Munro, Opt. Express **12**, 3605 (2004).
[33] Q. Zhan and J. R. Leger, Opt. Express **10**, 324 (2002).
[34] B. Ndagano, B. Perez-Garcia, F. S. Roux, M. McLaren, C. Rosales-Guzmán, Y. Zhang, O. Mouane, R. I. Hernandez-Aranda, T. Konrad, and A. Forbes, Nat. Phys. **13**, 397 (2017).
[35] B. Ndagano, I. Nape, M. A. Cox, C. Rosales-Guzmán, and A. Forbes, J. Lightwave Technol. **36**, 292 (2018).
[36] B. N. Simon, S. Simon, F. Gori, M. Santarsiero, R. Borghi, N. Mukunda, and R. Simon, Phys. Rev. Lett. **104**, 023901 (2010).
[37] M. McLaren, T. Konrad, and A. Forbes, Phys. Rev. A **92**, 023833 (2015).
[38] B. Ndagano, H. Sroor, M. McLaren, C. Rosales-Guzmán, and A. Forbes, Opt. Lett. **41**, 3407 (2016).
[39] J. Bell, Physics **1**, 195 (1964).
[40] J. F. Clauser, M. A. Horne, A. Shimony, and R. A. Holt, Phys. Rev. Lett. **23**, 880 (1969).
[41] F. Gori, G. Guattari, and C. Padovani, Opt. Commun. **64**, 491 (1987).
[42] I. A. Litvin, M. G. McLaren, and A. Forbes, Opt. Commun. **282**, 1078 (2009).
[43] Z. Bouchal, J. Wagner, and M. Chlup, Opt. Commun. **151**, 207 (1998).
[44] C. Rosales-Guzmán and A. Forbes, *How to Shape Light with Spatial Light Modulators* (SPIE Press, Bellingham, 2017).
[45] J. Turunen, A. Vasara, and A. T. Friberg, Appl. Opt. **27**, 3959 (1988).
[46] D. M. Cottrell, J. M. Craven, and J. A. Davis, Opt. Lett. **32**, 298 (2007).
[47] J. A. Davis, D. M. Cottrell, J. Campos, M. J. Yzuel, and I. Moreno, Appl. Opt. **38**, 5004 (1999).
[48] L. Marrucci, C. Manzo, and D. Paparo, Phys. Rev. Lett. **96**, 163905 (2006).
[49] F. Cardano, E. Karimi, S. Slussarenko, L. Marrucci, C. de Lisio, and E. Santamato, Appl. Opt. **51**, C1 (2012).
[50] R. J. C. Spreeuw, Found. Phys. **28**, 361 (1998).
[51] G.-S. Diego, B. Robert, Z. Felix, V. Christian, G. Markus, H. Matthias, N. Stefan, D. Michael, A. Andrea, O. Marco, and S. Alexander, Laser Photonics Rev. **10**, 317 (2016).
[52] A. Aiello, F. Toppel, C. Marquardt, E. Giacobino, and G. Leuchs, New J. Phys. **17**, 043024 (2015).
[53] C. V. S. Borges, M. Hor-Meyll, J. A. O. Huguenin, and A. Z. Khoury, Phys. Rev. A **82**, 033833 (2010).
[54] F. Töppel, A. Aiello, C. Marquardt, E. Giacobino, and G. Leuchs, New J. Phys. **16**, 073019 (2014).
[55] P. Chowdhury, A. S. Majumdar, and G. S. Agarwal, Phys. Rev. A **88**, 013830 (2013).
[56] W. F. Balthazar, C. E. R. Souza, D. P. Caetano, E. F. Galvão, J. A. O. Huguenin, and A. Z. Khoury, Opt. Lett. **41**, 5797 (2016).
[57] L. J. Pereira, A. Z. Khoury, and K. Dechoum, Phys. Rev. A **90**, 053842 (2014).
[58] A. Luis, Opt. Commun. **282**, 3665 (2009).
[59] M. A. Goldin, D. Francisco, and S. Ledesma, J. Opt. Soc. Am. B **27**, 779 (2010).
[60] X.-F. Qian and J. H. Eberly, Opt. Lett. **36**, 4110 (2011).
[61] K. H. Kagalwala, G. Di Giuseppe, A. F. Abouraddy, and B. E. A. Saleh, Nat. Photonics **7**, 72 (2013).
[62] B. Ndagano, R. Brüning, M. McLaren, M. Duparré, and A. Forbes, Opt. Express **23**, 17330 (2015).
[63] A. Forbes, *Laser Beam Propagation: Generation and Propagation of Customized Light* (CRC Press, Boca Raton, 2014).
[64] W. Wootters, Quantum Inf. Comput. **1**, 27 (2001).
[65] W. K. Wootters, Phys. Rev. Lett. **80**, 2245 (1998).
[66] G. Milione, H. I. Sztul, D. A. Nolan, and R. R. Alfano, Phys. Rev. Lett. **107**, 053601 (2011).
[67] G. Sorelli, V. N. Shatokhin, F. S. Roux, and A. Buchleitner, Phys. Rev. A **97**, 013849 (2018).
[68] S. Prabhakar, S. G. Reddy, A. Aadhi, C. Perumangatt, G. K. Samanta, and R. P. Singh, Phys. Rev. A **92**, 023822 (2015).
[69] B. S. Cirel'son, Lett. Math. Phys. **4**, 93 (1980).